Deep–Sea Research II 207 (2023) 105248

Contents lists available at ScienceDirect

Deep-Sea Research Part II

journal homepage: www.elsevier.com/locate/dsr2

Observed internal tides in the deep northwestern Pacific by argo floats

Yang Wang [a,b,c,d], Zhenhua Xu [a,b,c,e,f,*], Qun Li [g], Zhaohui Chen [b,h], Jia You [a,b,c], Baoshu Yin [a,b,c,e,f], Robin Robertson [i]

[a] CAS Key Laboratory of Ocean Circulation and Waves, Institute of Oceanology, Chinese Academy of Sciences, Qingdao, China
[b] Pilot National Laboratory for Marine Science and Technology, Qingdao, China
[c] Center for Ocean Mega-Science, Chinese Academy of Sciences, Qingdao, China
[d] Key Laboratory of Marine Science and Numerical Modeling, Ministry of Natural Resources, Qingdao, China
[e] College of Earth and Planetary Sciences, University of Chinese Academy of Sciences, Beijing, China
[f] CAS Engineering Laboratory for Marine Ranching, Institute of Oceanology, Chinese Academy of Sciences, Qingdao, 266071, China
[g] Polar Research Institute of China, Shanghai, China
[h] Key Laboratory of Physical Oceanography/Institute for Advanced Ocean Science/Frontiers Science Center for Deep Ocean Multispheres and Earth System, Ocean University of China, Qingdao, China
[i] China-Asean College of Marine Science, Xiamen University Malaysia, Sepang, Malaysia

A R T I C L E I N F O

Keywords:
Internal tide
Argo
Northwestern pacific
Tidal dissipation
Energy decay
Parameterization

A B S T R A C T

This study aims to extract the observed internal wave signals in the northwestern Pacific from Argo floats with Iridium-telecommunication that can directly measure the hourly temperature, salinity and pressure near 1000 dbar. Vertical displacements and spectral features of internal tides can be interpreted from Argo float data. More than 10,000 parking-phase observations of 252 Argo floats were used to estimate their spatial-temporal characteristics. Vertical displacements attributed to internal tides exceeded 30 dbar near energetic sources, such as the Luzon Strait, Izu ridge, Mariana Arc and Palau. The observed internal tides feature both seasonal and spring-neap cycles corresponding to barotropic tidal variations. The diurnal and semidiurnal peaks in the energy spectra differed with latitude in related to different internal wave properties. Particularly, energetic local-trapped diurnal internal tides (topographic waves) occurred at 33°N near Izu Ridge, which is poleward of diurnal critical latitude. The internal tidal energy was calculated by theoretical fitting the vertical displacements from one layer to the full-depth water. The observed e-folding decay scales of the semidiurnal internal tidal energy were estimated as ~550–950 km in the deep basin. The Argo parking data provide a unique view for observing the basin-scale pattern and energy sink of deep-ocean internal tides, which could supplement the widely-used surface altimetry observations and contribute to a more accurate parameterization of tidal mixing.

1. Introduction

Internal tides play an important role in numerous oceanic processes, such as vertical particle transport and acoustic propagation (Sharples et al., 2007; Wang et al., 2007; Duda et al., 2013; Shanks, 2021). It has been widely emphasized that internal tides contribute significantly to ocean mixing, which maintains the basin scale meridional overturning circulation (Munk and Wunsch, 1998; Oka and Niwa, 2013; Wang et al., 2016). Furthermore, a key task for developing climate-scale models is to parameterize the subgrid-scale internal tides and associated mixing, which cannot be explicitly resolved (Mackinnon et al., 2017; Vic et al., 2019; Fox-Kemper et al., 2019; Zhang et al., 2022). Therefore, a better understanding of internal tides, both regionally and globally, could facilitate the understanding of their impacts on other oceanic processes, as well as their connection to climate change (Melet et al., 2016; Alford et al., 2015; Whalen et al., 2020).

Much interest regarding internal tides has focused on their energy redistribution after generation (Alford, 2003; Rainville and Pinkel, 2006; Alford et al., 2007, 2016, 2019; de Lavergne et al., 2019; Lahaye et al., 2020; Buijsman et al., 2020; Wang et al., 2021). Internal tides can propagate hundreds to thousands of kilometers in the open ocean and throughout the water column, inducing spatial variable patterns, both horizontally and vertically (Arbic et al., 2012; Zhao, 2014; Wang et al., 2021; Zhao et al., 2021). These long-range radiation processes remarkably spread internal tide signals and redistribute internal tidal energy (Wilson, 2011; Kelly et al., 2013; Xu et al., 2016), resulting in the

* Corresponding author. CAS Key Laboratory of Ocean Circulation and Waves, Institute of Oceanology, Chinese Academy of Sciences, Qingdao, China.
E-mail address: xuzhenhua@qdio.ac.cn (Z. Xu).

https://doi.org/10.1016/j.dsr2.2022.105248
Received 12 March 2022; Received in revised form 19 September 2022; Accepted 19 December 2022
Available online 23 December 2022
0967-0645/

significant spatiotemporal variations from the Garrett-Munk spectrum (GM76) which describes the quasi-universal background internal wave spectral level (Garrett and Munk, 1975; Cairns and Williams, 1976; Klymak and Moum, 2007; Hennon et al., 2014; Whalen et al., 2020). The low-mode internal tidal energy can further cascade to high modes or turbulence through topographic scattering (Xu et al., 2013; Legg, 2014; Waterhouse et al., 2017; Zeng et al., 2021) and wave-wave interactions (Mercier et al., 2012; Van Haren et al., 2019; Jithin et al., 2020). The subinertial eddies may also contribute to the instability of low-mode internal tides (Kerry et al., 2014; Buijsman et al., 2017).

Direct observations of basin-scale internal tides remain a challenge to oceanographers. Compared to the large-scale low-frequency circulations, their smaller horizontal scales, more complex vertical structures, high oscillating frequencies, and temporal variations require observations on much finer spatial and temporal scales (Bruno et al., 2000; Klymak et al., 2011; Rainville et al., 2013; Alford et al., 2015; Chang et al., 2019). In-situ mooring data with high sampling frequencies have been used to analyze internal tidal variability, but owing to the high cost, the data are too sparse to provide a basin-scale observed map of internal tides (Alford, 2003; Huang et al., 2018). For this reason, numerical simulation has been widely used for studying internal tides, on both regional and global scales (e.g. Simmons et al., 2004; Niwa and Hibiya, 2004; Buijsman et al., 2012; Xu et al., 2021).

Historically accumulated altimetry data have been used to investigate internal waves, primarily internal tides (Ray and Mitchum, 1996; Mitchum and Chiswell, 2000; Ray and Cartwright, 2001). Recently, regarding the basin-scale map, the global propagation pattern of mode-1 internal tides have been constructed by conducting a plane wave fitting method (Zhao et al., 2016; Zhao, 2019; Zaron, 2019). Zhao (2018) also extracted the global mode-2 semidiurnal patterns. Nevertheless, only the coherent portion of the internal tides could be extracted based on altimetry data (Zhao et al., 2016). Moreover, the altimeter only sensed the surface signal of internal tides. Uncertainties still exist regarding the submarine characteristics such as the internal tidal vertical oscillating magnitude, as well as their temporal variations.

Here, we estimate the basin-scale map of internal tides using drift data recorded by Iridium-telecommunication Argo floats which have a broad spatial coverage and record the high-frequency (hourly) information near 1000 dbar. Pioneer work by Hennon et al. (2014) first used this type of float data to examine the distribution and variability of internal tides. These floats usually cycle vertically between 2000 dbar and the sea surface with a ~10-day period and record vertical profiles when rising to the surface (Roemmich et al., 2004). They also measure the hourly temperature, salinity and pressure during their parking phase at ~1000 dbar. It should be noted that the 1000 dbar depth approximately coincides with the permanent pycnocline's lower bound (Fig. 1, Feucher et al., 2016) and approximately corresponds to the maximum displacement of the mode-1 internal tides in the open ocean (Rainville et al., 2013; Hennon et al., 2019). Therefore, the hourly data can capture the internal tidal fluctuations at this depth (Hennon et al., 2014).

Our focus is in the northwestern Pacific (NW Pacific), which is globally one of the most energetic areas of internal tides (Kantha and Tierney, 1997; Niwa and Hibiya, 2011; Zhao et al., 2016; Li et al., 2015, 2017; Savage et al., 2017; Zaron, 2019; Song and Chen, 2020; You et al., 2021). Recently, internal waves in the NW Pacific are found to have considerable imprints on temperature fluctuations using rapid-sampling deep profiling floats (Gao et al., 2021). It should be noted that the magnitudes of internal tides are usually much larger than that of near-inertial waves at 1000 dbar in the open ocean (Hennon et al., 2014). Previous in-situ observational studies in the NW Pacific have been focused on the hotspot Luzon Strait (Alford et al., 2011; Rainville et al., 2013; Zhao 2014; Pickering et al., 2015; Alford et al., 2015). Regarding the basin-scale map of internal tides in the NW Pacific, studies were mainly based on numerical modeling and altimetry data. Multiple semidiurnal internal tidal sources, such as the Luzon Strait, Ryukyu Islands, Bonin Ridge and the Mariana Arc, have been revealed to radiate long-distance propagating internal tides into the deep basin (Niwa and Hibiya, 2001, 2004; Zhao and D'Asaro, 2011; Kerry et al., 2013; Varlamov et al., 2015; Zhao et al., 2016; Wang et al., 2018), while diurnal internal tides mainly radiated from Luzon Strait and have larger propagation speeds than semidiurnal (Zhao, 2014; Zaron, 2019). Many aspects of the characteristics of internal tides in the NW Pacific, such as their temporal variability and energy sinks, remain unclear.

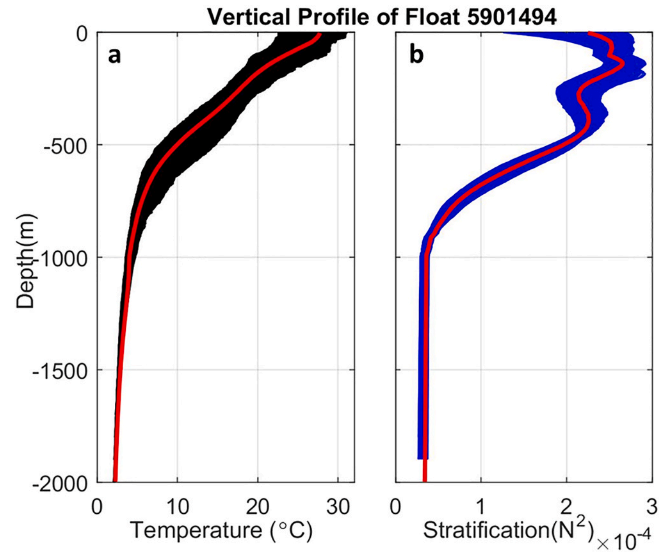

Fig. 1. Vertical profile from Argo float. (a) The black color indicates the variation range of vertical profiles of temperature from Float 2901494, the red line indicates the averaged value. (b) The blue color indicates the variation range of vertical profiles of stratification; the red line indicates the averaged value.

In this study, we reveal the spatiotemporal variability of internal waves, primarily at tidal frequencies, in the NW Pacific using Iridium-telecommunication Argo data. The data processing and method is explained in Section 2. Detailed results derived from the Argo observations are presented in Section 3. Section 4 provides discussion and summary.

2. Data and method

2.1. Data

The Argo Program has provided high-quality observational temperature and salinity data in the ocean's upper 2000 m in the past two decades, with a global array of over 4000 profiling floats (Roemmich et al., 2019). A typical work cycle of an Argo float consists of diving to the parking depth, usually 1000 dbar, drifting at the parking depth for ~9 days (parking-phase), sinking to 2000 dbar, rising to sea surface and profiling temperature and salinity along the way, and finally transmitting the data with the position information to the data center via satellite (Fig. 2a, Roemmich et al., 2004). The cycle repeats about every 10 days, while it can be several days for faster cycling floats. Some of these Argo floats are implemented with Iridium satellite telecommunication system and thus are able to store and transmit more data than others (henceforth, Iridium-telecommunication Argo floats, Wu et al., 2011; Hennon et al., 2014). These floats record hourly temperature and salinity as a function of pressure during the parking-phase period at the drifting depth, providing an unprecedented database for examining the variability of tidal-frequency internal waves.

In this study, we use more than 10,000 parking-phase observations from 252 Iridium-telecommunication Argo floats. These Iridium-telecommunication Argo floats were deployed and operated in the NW Pacific. The trajectories of these floats covered the entire NW Pacific

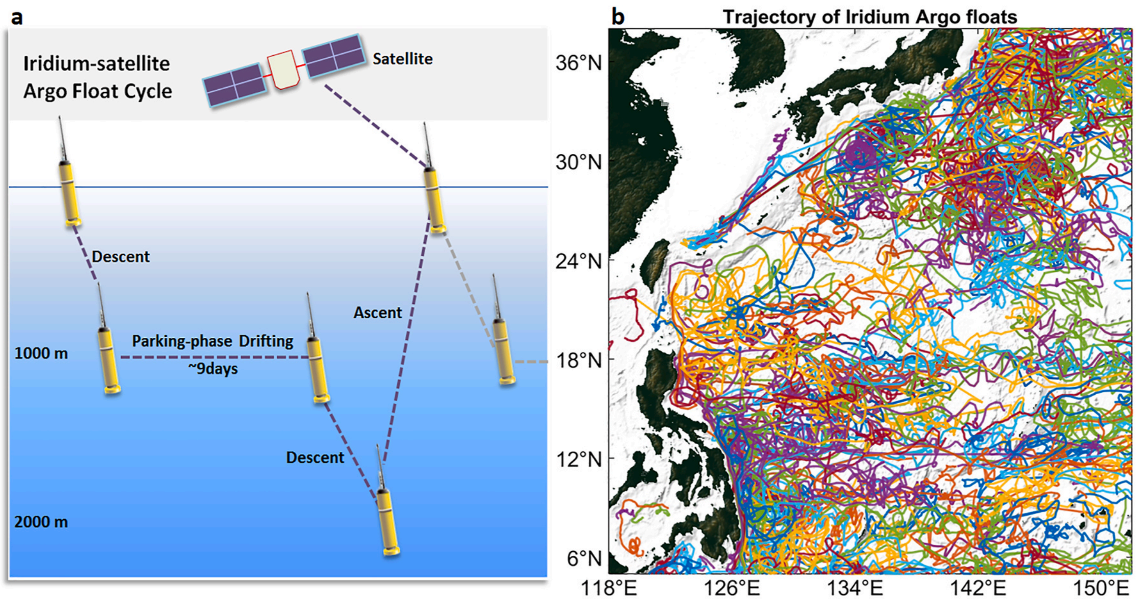

Fig. 2. (a) Schematic for the working cycle of Iridium-telecommunication Argo floats (redrawn from https://argo.ucsd.edu/about/); they measure and reserve hourly temperature, salinity and pressure data during the parking-phase; (b) Trajectories (color lines) of Iridium-telecommunication Argo floats in the NW Pacific.

basin (Fig. 2b). Thus, we can extract information for the basin-scale pattern of internal tides.

2.2. Methods

The Iridium-telecommunication Argo floats drift freely near the parking depth. The hourly potential density calculated from the hourly temperature, salinity and pressure could indicate the isopycnal variability. Vertical isopycnal displacements can be derived by the potential density fluctuations and the vertical gradient of potential density (Equation (1)). The total displacements should be attributed to internal gravity waves. Because the parking pressures of the Iridium-telecommunication Argo floats selected for the present study are 1000 dbar, the effect of near-inertial waves are usually minor at that depth (Alford et al., 2016). The NW Pacific also has been suggested to generate energetic internal tides. Therefore, the hourly fluctuations of the derived isopycnal displacements are thought to be mainly caused by internal tides (Fig. 1), although the spectrum is generally in the similar form as Garrett-Munk spectrum.

The isotherm displacement was used to translate the temperature fluctuations in the study of Hennon et al. (2014). Since the potential density is more monotonic in depth than temperature, the isopycnal displacement is used to represent the potential density fluctuations in the present study. Due to the quasi-Lagrangian nature of the Argo floats, we did the analysis of spectra, temporal variability in the Lagrangian framework. The spatial map of displacements is derived by time-averaging the hourly values in geographical bins with size of 0.8° × 0.8°.

We calculated the hourly isopycnal displacements for each parking period using

$$\eta_{Pden}(t) = \frac{\rho(t) - \overline{\rho}}{\mu} \tag{1}$$

in which $\mu = \frac{d\rho_r}{dp}$ is the vertical gradient of potential density, where ρ_r is the reference potential density derived from the profile data. $\rho(t)$ is the calculated hourly potential density using the hourly temperature, salinity and pressure, and $\overline{\rho}$ is the time average potential density for each parking-phase period. Both the reference potential density and hourly potential density are calculated with the Gibbs Sea Water toolbox (McDougall and Barker, 2011).

The floats are not isobaric and possess small vertical motions, $\eta_{Float}(t)$, which need to be removed from the $\eta_{\mathrm{Pden}}(t)$. The $\eta_{Float}(t)$ is defined as (Hennon et al., 2014)

$$\eta_{Float}(t) = P(t) - \overline{P} \tag{2}$$

where $P(t)$ is the hourly collected pressure during the parking-phase period and $\overline{P}$ is the time averaged value for each parking period. Then we can get the corrected isopycnal displacement, $\eta(t)$

$$\eta(t) = \eta_{Pden}(t) - \eta_{Float}(t) \tag{3}$$

Quality controls were implemented following Hennon et al. (2014) to reduce the unreasonable estimates for the data analysis: 1) the vertical gradient of potential density was derived using the local-mean profiles of temperature and salinity. Unreasonable gradients caused by the measurement bias were discarded; 2) the parking depth for some of the Argo float were significantly different than 1000 dbar. Data from these floats were not included in the estimation of displacements and energy; 3) the vertical movement of float that deviates >50% of the isopycnal displacement was not included. Furthermore, some unreasonable values, which were not a result of the internal waves but by the spatial varying subinertial processes, were removed using a detrend method.

To illustrate the validity of the data and method used in our study, we give an example of analysis for a selected Iridium-telecommunication Argo float (Float number: 2901494). This float was deployed in the east of Luzon Strait on September 2011 and measured data until February 2016. The trajectory of float 2901494 is presented in Fig. 3a and part of the trajectory (plotted in blue) was well within the radiation range of internal tides from Luzon Strait and Miyako Strait (Niwa and Hibiya, 2004; Wang et al., 2018). This float drifted within a relatively smaller region over a long period and thus can characterize the time variability for this region. We calculated the hourly vertical displacements of each parking-phase period for this float (Fig. 3b). A Butterworth filter with cutoff frequency bands at 0.8–1.2 cpd and 1.7–2.3 cpd were used to extract the diurnal and semidiurnal signals for this float, respectively.

Periodic features were evident in both the raw calculated displacement values (blue line) and the band-passed (0.8–2.3 cycle per day) filtered signal (red line). Furthermore, a spring-neap-like cycle is clearly present (black dashed line). Notably, the values of the band-pass filtered

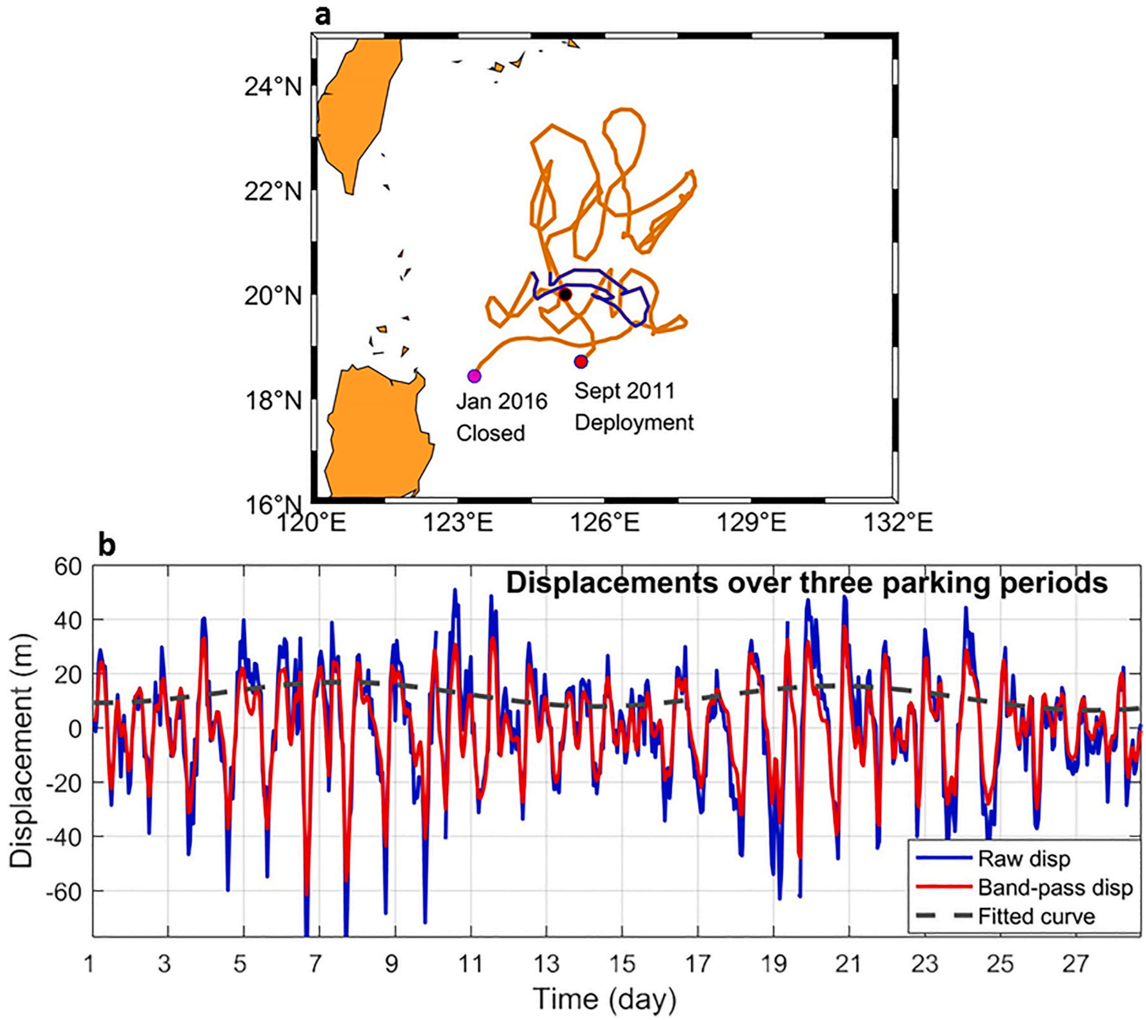

Fig. 3. (a) Trajectory of a selected float 2901494, the black dot indicates the location during the period plotted in (b), partial trajectory in blue color indicates the one-year long data used for seasonal analysis; (b) Time series of vertical displacements over three parking-phase periods (about a month), the blue line indicates the raw displacements, the red line denotes the band-passed filtered values which include the diurnal and semidiurnal-band signals. The gray dashed line is the fitted curve of the displacement magnitude using a polynomial fit, which indicates a spring-neap period.

signals account for most of the displacement variance, further proving the dominant role of internal tides in generating the vertical displacements near the parking depth.

3. Results

3.1. Spatial map of the vertical displacements

The long-time-mean Iridium-telecommunication Argo float vertical displacements, averaged into geographical bins (Fig. 4a), show significant spatial variability. Whereas relatively smaller magnitude displacements are widely distributed throughout the NW Pacific's deep basin, enhanced vertical displacements, ~30–50 dbar, occur near rough topographic features, including Luzon Strait (LS), Miyako Strait (MY), Izu Ridge (IZU), Mariana Arc (MA) and Palau (PA). All of these rough topographic features are well-known for strong internal tidal generation (Fig. 4b–d) (Kerry et al., 2013; Zhao, 2014; Varlamov et al., 2015; Wang et al., 2018; de Lavergne et al., 2019), to which the observed enhanced vertical displacements can be attributed.

In the deep basin, vertical displacement magnitudes decreased with increasing distance from the rough topographic features at the boundaries. Typical magnitudes were ~10–20 dbar or less in the middle and northeastern regions of the NW Pacific basin. A notable exception was the mid-western part of the basin (yellow rectangle in Fig. 4a), where the vertical displacements were enhanced even far from rough topography. The strong vertical displacements there were quite possibly caused by constructive interference between internal tides from the LS and MY. The constructive interference remarkably enhanced the baroclinic SSH (sea surface height) and internal tidal energy flux (Zhao, 2014; Wang et al., 2018). Another possible explanation is that these intensified vertical displacements could be attributed to the spring-neap variability. Previous numerical results showed that the subtidal processes will result in the incoherence of internal tides (Buijsman et al., 2017) and refract the propagation path of internal tides (Wang et al., 2021). These effects may further influence the magnitude of internal tidal isopycnal displacements. The observed semidiurnal internal tides by float 2901494 showed some inconsistency with the barotropic tide from the Luzon Strait, which may be induced by the multi-wave interference and mesoscale eddies. Since the Argo observations are not point-fixed, the observations may have occurred exactly during a spring tide.

3.2. Seasonal and spring-neap variability

Argo floats usually drift over long distances during their lifetime, up to orders of 1000 km (Fig. 2a), making it difficult to investigate the internal tidal seasonal variability for a fixed point. To investigate

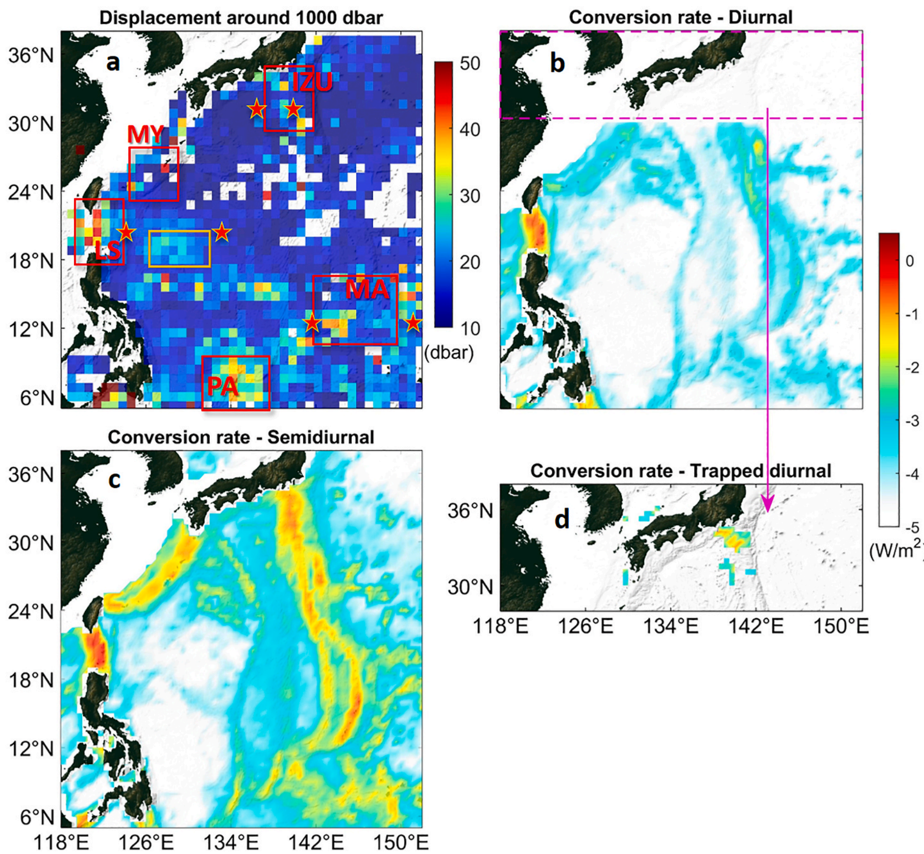

Fig. 4. (a) Argo-derived vertical displacements (unit: dbar). The red rectangles indicate the regions (LS: Luzon Strait, MY: Miyako Strait, IZU: Izu ridge, MA: Mariana Arc, PA: Palau) which have been revealed to be generation sites of internal tides. The magenta pentagrams represent the locations selected for spectral analysis. The red rectangle indicates the enhanced displacements in the northwestern part of the NWP basin; (b) Barotropic to baroclinic conversion rate of diurnal internal tide from de Lavergne et al. (2019), the dashed line indicates the critical latitude for diurnal internal tide.; (c) As in (b) but for semidiurnal internal tide, the conversion rate is plotted in log scale. (d) Conversion rate for the trapped diurnal internal tides to the north of 30° N from Wang et al. (2021). Note that the conversion rate is plotted in log scale.

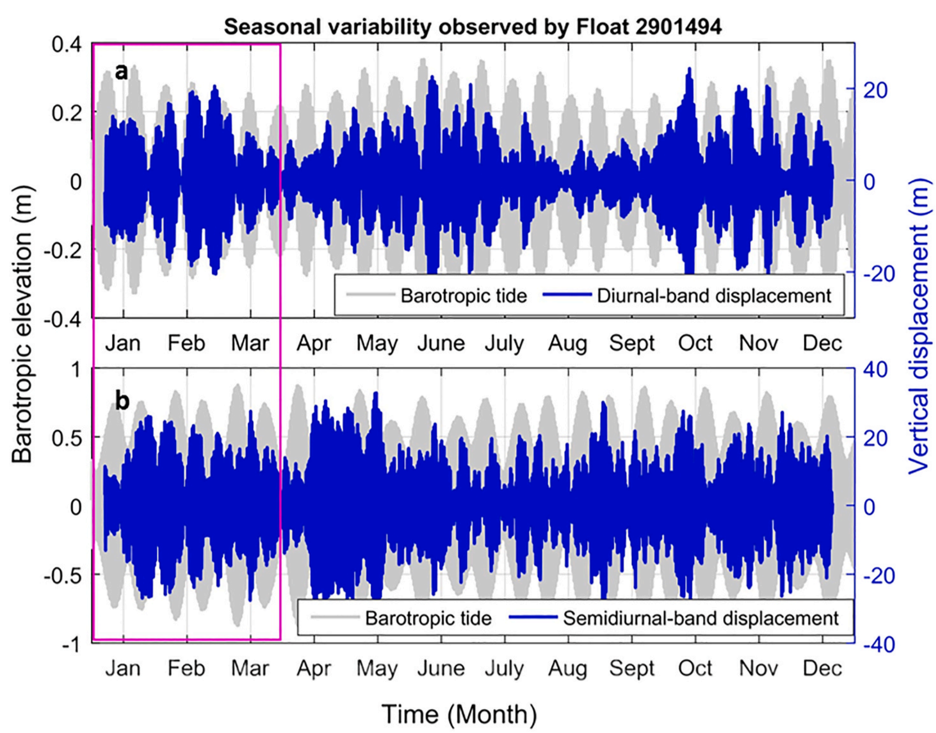

Fig. 5. (a) Yearly time variability of diurnal-band internal tides. The gray shadow represents the barotropic tide magnitude (near the Luzon Strait) and the blue shadow is the observed vertical displacements. (b) As in (a) but for semidiurnal-band internal tides. The magenta rectangle indicates the time period as shown in Fig. 7 to illustrate the spring-neap variability.

temporal variability, we chose an Argo float (NO. 2901494), which was relatively stationary over a long-time period and did not cover a large region (Fig. 3a) during a year. Previous studies for the area of this float suggested that internal tides in this region mainly radiate from the LS and MY (Kerry et al., 2013, 2014; Zhao, 2014; Varlamov et al., 2015).

The observed diurnal-band displacements exhibited evident seasonal variability in this region, with stronger magnitudes during summer and winter (Fig. 5a), approximately twice as large as during spring and autumn. However, the semidiurnal-band internal tides do not exhibit an apparent seasonal variability (Fig. 5b). One important contributor to the seasonal variability of diurnal-band internal tides may be the barotropic tidal forcing. Considering that the internal tides observed by Float 2901494 mainly radiate from the Luzon Strait, we compared the barotropic tidal forcing (Fig. 5 gray shading) at LS with the float's internal tidal signals (Fig. 5 blue shading). The seasonal tendency coincided quite well with the barotropic tidal forcing, especially for the diurnal-band internal tides (Fig. 5a). This finding reinforced the view that the seasonal nature of internal waves generated at Luzon Strait is highly modulated by barotropic tidal forcing, which is consistent with previous mooring observations (Xu et al., 2014; Cao et al., 2017).

We further performed a cross-spectrum analysis to investigate the relation between the internal tides and barotropic tides (Fig. 6a). The cross spectrum showed that the internal tides were highly correlated with the LS barotropic tides. The correlation coefficients for diurnal and semidiurnal bands reached over 0.8 and 0.6, respectively (Fig. 6a). Relatively significant peaks can be also seen on the spring-neap and higher harmonics.

By zooming in on the time-series in Fig. 5 (magenta rectangle), we can further investigate the spring-neap variability of the internal tides (Fig. 7a and b, for the diurnal and semidiurnal-bands, respectively). The spring-neap variability of internal tides was also consistent with the barotropic tidal forcing at LS, with the diurnal internal tides being more consistent. Phase lags existed between the internal tidal signal and barotropic forcing. The phase lags for diurnal are more stationary, which are around ~1–2 days as shown in Fig. 7a. The distance from LS to the float is about 450–600 km as shown in Fig. 3a. The phase speed for diurnal internal tide is ~4 m/s in this region (Zhao, 2014) and allows propagation distance ~350–700 km within 1–2 days. This kind of lagged phenomenon had been well observed by fixed-location moorings (Alford and Zhao, 2007).

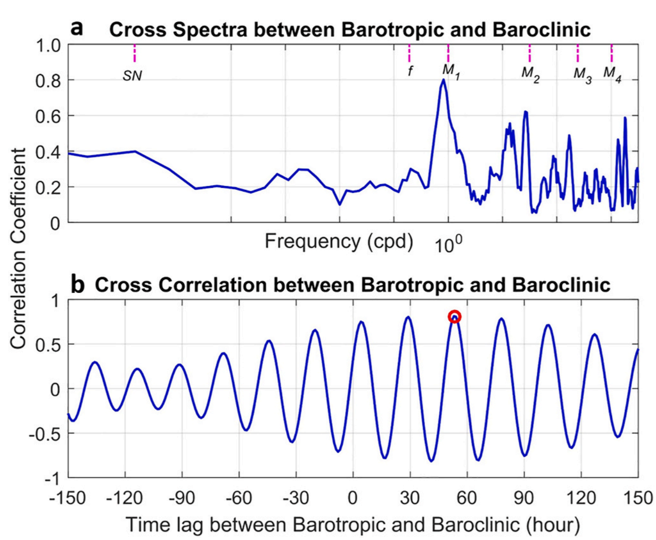

Fig. 6. (a) The cross spectrum for the barotropic tide and internal tide as shown in Fig. 5a. (b) The lead-lag correlation between the diurnal barotropic component and band-passed diurnal internal tide as shown in Fig. 7b. The red circle indicates the time lag about 47 h corresponding to the largest correlation coefficient.

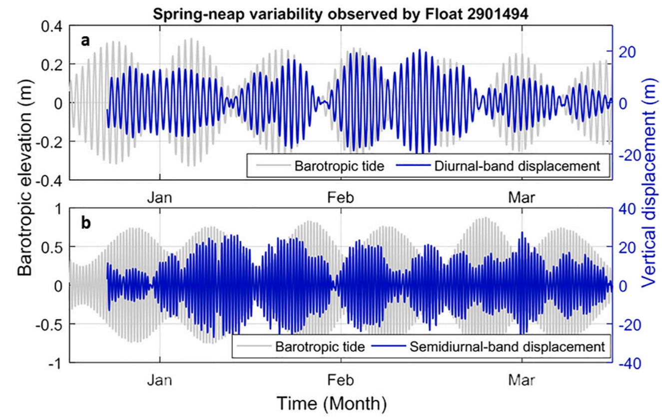

Fig. 7. (a) Time-series (as indicated in Fig. 5 by the magenta rectangle) of the diurnal-band barotropic tide and observed vertical displacements. The gray shadow represents the barotropic tide magnitude and the blue shadow is the observed vertical displacements. (b) As in (a) but for semidiurnal band internal tides.

The lead-lag correlation was presented to further confirm the relation between the barotropic tides at LS and the diurnal internal tides (Fig. 6b). The largest correlation coefficient corresponded to a time lag about 47 h between the LS diurnal barotropic tides and diurnal internal tide observed by float 2901494. This is consistent with the above mentioned estimation that the diurnal internal tides from LS can propagate to the observed area within ~1–2 days.

Variations of semidiurnal internal tides were relatively more complex. Unlike the diurnal internal tides which were dominated by those generated in LS, semidiurnal internal tides from both the LS and MY can reach this area (Niwa and Hibiya, 2004; Arbic et al., 2012; Varlamov et al., 2015; Wang et al., 2018). As a result, the semidiurnal internal tide signal for a single float may be composed of multiple semidiurnal signals from LS and MY, resulting in a more complex spring-neap variability of semidiurnal-band internal tides.

3.3. *Spatially variable power spectra*

The internal wave spectra represent the energy redistribution of internal wave energy over a wide range of frequencies and are shaped by wave-wave interactions. In this section, we examine the relationships between the observed internal wave spectrum and the expected quasi-universal Garrett–Munk displacement spectrum (1975). Due to the quasi-Lagrangian nature of the Argo floats (Hennon et al., 2014), we computed the power spectra in the Lagrangian framework along the drifting trajectories (Yu et al., 2019). Displacements from several individual parking periods were combined, with assigning the missing part as local mean value, to get longer records to improve the resolution of the spectrum. 95% confidence levels were presented to distinguish the significant peaks (Fig. 8). The data used are limited by their shorter length for each segment. In addition, the missing values during two segments also decrease the spectrum resolution. Therefore, it is difficult to distinguish the K_1 and O_1 components (as well as M_2 and S_2 components). Here we use the M_1 and M_2 to represent the diurnal and semidiurnal bands. M_3 and M_4 represent their higher harmonics.

The power spectra vary significantly with location and latitude (Fig. 8). We chose six representative points for the spectral analysis (see magenta pentagrams in Fig. 4a), with three locations each selected near the source regions and in the far field. Generally, spectra near source regions had evident peaks at the diurnal and semidiurnal frequencies (Fig. 8a,c,e). Notable higher harmonics such as M_3 and M_4 were also more evident at the near-source locations (Fig. 8a,c), potentially contributing to local dissipation. The strong variance near the source region was likely attributed to strong internal tide generation. The

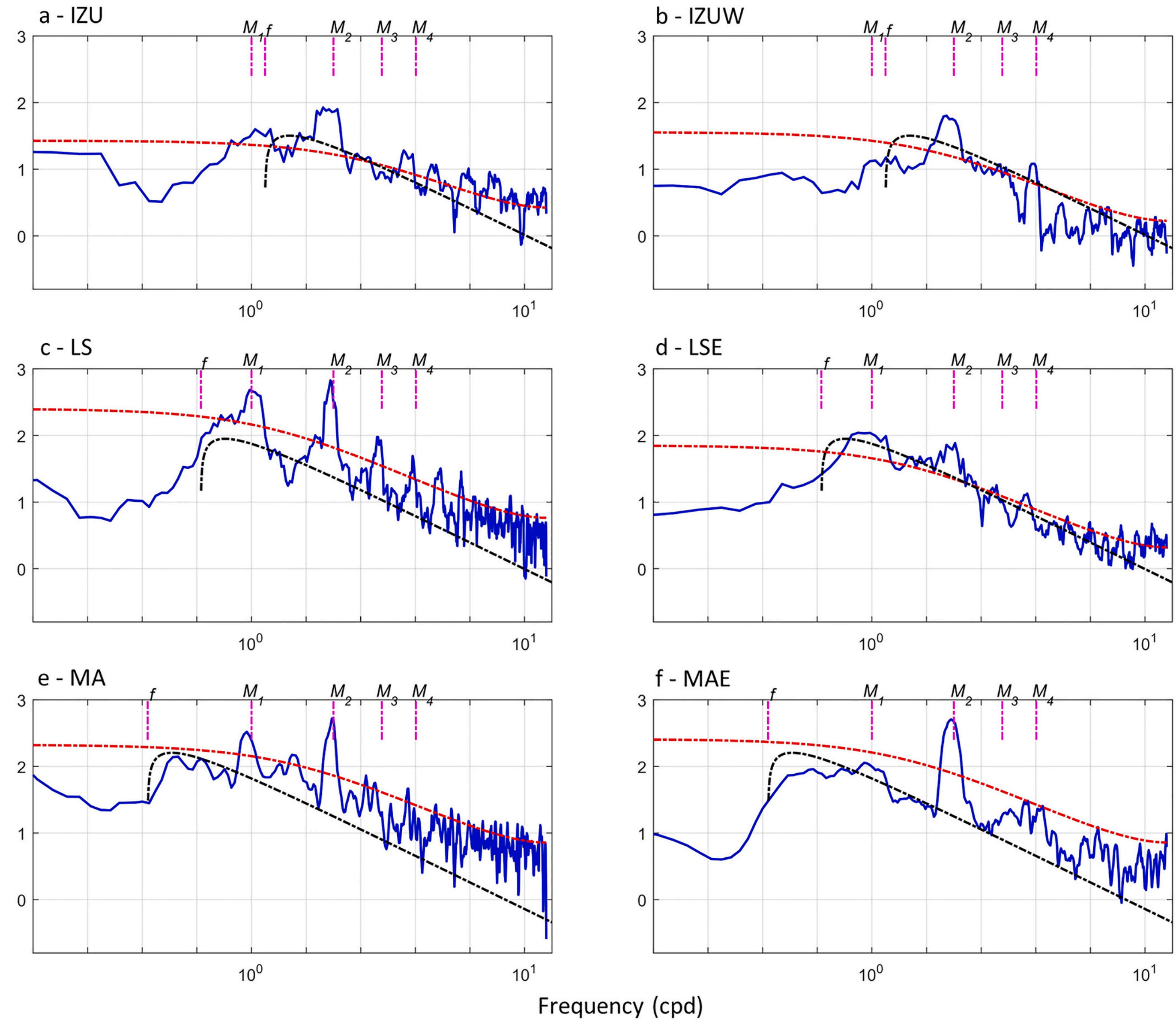

Fig. 8. The power spectra of the observed vertical displacements at the selected points in Fig. 4a (LZ: near Luzon strait; LZE: east of LS; IZUW: west of IZU ridge, IZU: near IZU ridge; MAE: east of Mariana arc, MAW: west of Mariana arc), the black dash lines indicate the GM spectra and the red dashed lines denote 95% confidence levels, both the y-axis and x-axis are plotted in log scale. M1 and M2 represent the diurnal and semidiurnal bands, respectively. M_3 and M_4 represent their nonlinear harmonics (3 cpd and 4 cpd).

spectra in the far field (far away from the generation sources), however, were much smoother and matched better with the GM spectra (Fig. 8b,d, f). This is consistent with the simulated and observational results in the Indonesian seas (Robertson, 2011) and South China Sea basin (Xie et al., 2010).

Previous studies suggested that MA, LS and Izu are all energetic generation sites for semidiurnal internal tides (Niwa and Hibiya, 2004; Kerry et al., 2013; Wang et al., 2018; Masunaga et al., 2017). Therefore, it is not surprising that all three near-source locations were characterized by strong semidiurnal peaks. The intriguing phenomenon is that diurnal signals were also identified near the three sources (Fig. 8a, c, e). The diurnal signals in the three near-source locations are attributed to different processes.

Specifically, for the point near LS, the observed power spectral density showed comparable magnitudes for the diurnal and semidiurnal internal tides (Fig. 8c), which is consistent with the spectral characteristics for LS (Jan et al., 2007, 2008; Alford et al., 2011; Xu et al., 2014; Pickering et al., 2015). In the near-source region of the MA, both diurnal and semidiurnal peaks were significant (Fig. 8e). The MA is characterized as a strong semidiurnal internal tide generation site, but generates relative weaker diurnal internal tides (Fig. 4b and c) (Niwa and Hibiya, 2011; Müller, 2013). The long-range propagated diurnal internal tides from LS can reach the southern part of west MA basin, which contributed to the local diurnal internal tidal energy (Zhao, 2014). In addition, notable diurnal signals were also found in the vicinity of the Izu Ridge (Fig. 8a). The latitude of Izu Ridge is poleward of the diurnal critical latitudes (~30°N and 27.6°N for the K_1 and O_1 constituents, respectively). Consequently, the generated diurnal internal tides cannot freely propagate and will be trapped locally or propagate anti-cyclonically around the ridge as topographic waves, leading to enhanced local dissipation (Falahat and Nycander, 2015; Dong et al., 2019; Musgrave et al., 2017; Masunaga et al., 2017).

3.4. Locally-trapped diurnal internal tides

The locally trapped diurnal internal tides near Izu ridge was further investigated. In our study area, according to previous numerical and theoretical reports, the trapped diurnal internal tides were mainly generated around the Izu ridge (Niwa and Hibiya, 2011; Falahat and Nycander, 2014; Masunaga et al., 2017).

The Argo float 2902052 drifted through the Izu ridge during April 2017–June 2017 (Fig. 9a), providing a good data record to investigate the features of the trapped diurnal internal tide. The magnitude of diurnal internal wave decayed rapidly away from the source site (Fig. 9c). The semidiurnal decayed much more slowly, and can propagate longer distance (Fig. 9b). This phenomenon indicates that the diurnal internal waves are locally trapped around the topography.

The locally trapped diurnal internal waves (internal Kelvin waves) follows the relation

$$c = L_e f$$

where c is the propagation speed, L_e represents the e-folding distance of the wave magnitude away from the topography, and f is the coriolis frequency (Masunaga et al., 2017). The L_e of the observed diurnal internal wave was about 12.8 km (Fig. 9c). We estimated the propagation speed of this trapped wave c is about 1.02 m/s. The e-folding distance and propagation speed for the observed trapped diurnal internal wave is comparable to previous model estimations in this region (Masunaga et al., 2017).

3.5. An estimation of basin-scale mode-1 energy

These observations are unique and valuable, as they provide us an unprecedented opportunity to estimate the basin-scale pattern of internal tidal energy, which is important for quantifying the remote tidal dissipation in the deep basin. However, the observations are not point-fixed and many of the floats did not follow a typical work cycle but park at 1000 dbar only for one or a few days, making it difficult to separate the semidiurnal and diurnal signals using the band-pass method. The internal tidal SSH (a) and the interior displacements (η) follows the relation (Zhao et al., 2016):

$$\mathrm{a} = \frac{\eta_0}{\mathrm{g}} \int_{-\mathrm{H}}^{0} \mathrm{N}^2 \varphi(\mathrm{z}) \mathrm{dz} \tag{4}$$

where a is the sea surface height, η_0 is the maximum interior displacement and $\varphi(z)$ is the vertical structure of interior displacement. $\eta_0\varphi(z)$ is the interior displacement at different water depth. This equation indicates that the SSH has a linear relation with the interior displacement. Based on this relation, the internal tide energy has been well derived from the altimetry observations (Zhao and Alford, 2009; 2016). Here, we estimated the ratio of semidiurnal/diurnal at each geographical bin (shown in Fig. 4a) using the altimetry observed internal tidal SSH by Zhao (2019) and Zaron (2019). Further, according to the above equation (4), we separated the semidiurnal and diurnal isopycnal displacements at each bin accordingly.

The energy of long-distance propagating internal tides is mainly retained in the mode-1 component (Zhao et al., 2016; Alford et al., 2019). We determined the mode-1 vertical structure using the time-mean stratification by solving the eigenvalue equation (Zhao and Alford, 2009; Rainville et al., 2013):

$$\frac{d^2\Phi(z)}{dz^2} + \frac{N^2(z)}{C^2}\Phi(z) = 0 \tag{5}$$

where $\Phi(z)$ is the eigenfunction, describing the mode-l structure of the vertical velocity and displacements (Gill 1982).

As we obtained the shape of the mode-1 internal tide at all depths (Fig. 10b and c), then the full-depth displacements are calculated as $\eta_0\varphi(z)$. We calculated the available potential energy (APE) following Martini et al. (2007)

$$APE = \frac{1}{2}\rho_0 \int_{-H}^{0} N^2\eta^2 dz \tag{6}$$

Except for some interference regions, the progressive wave dominated in the NW Pacific (Fig. 10 of Zhao et al., 2016), the relation between APE (available potential energy) and HKE (horizontal kinetic energy) for progressive internal wave is

$$\frac{\mathrm{HKE}}{APE} = \frac{\omega^2 + f^2}{\omega^2 - f^2} \tag{7}$$

in which ρ' is the perturbation density and ω is the frequency of semidiurnal internal tide. Since the diurnal internal tide becomes subinertial poleward of critical latitude (where diurnal frequency equals f), Eqn (7) is not applicable anymore. Therefore, we only present the estimated energy for the semidiurnal and the progressive component of diurnal internal tides in this study (Fig. 10e and f).

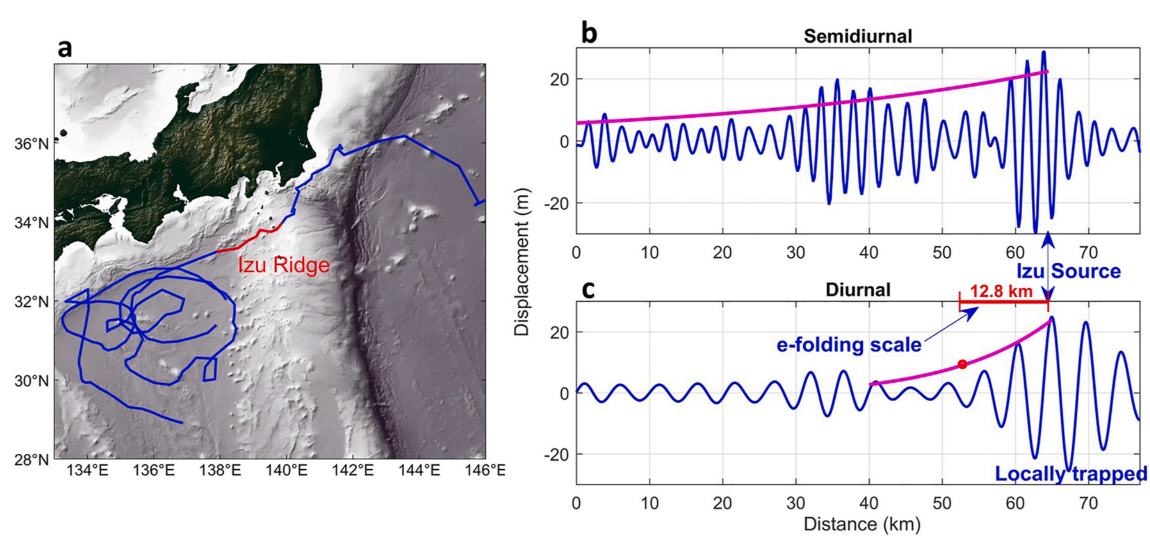

Fig. 9. (a) Blue curve indicates the trajectory of float 2903052, the red curve indicates the record presented in (b) and (c). (b) Magnitude of semidiurnal internal waves, the magenta curve indicates the exponential fit of the variation trend of the internal tide magnitude. (c) As in (b), but for diurnal internal waves. The red line indicates the e-folding scale of the magnitude.

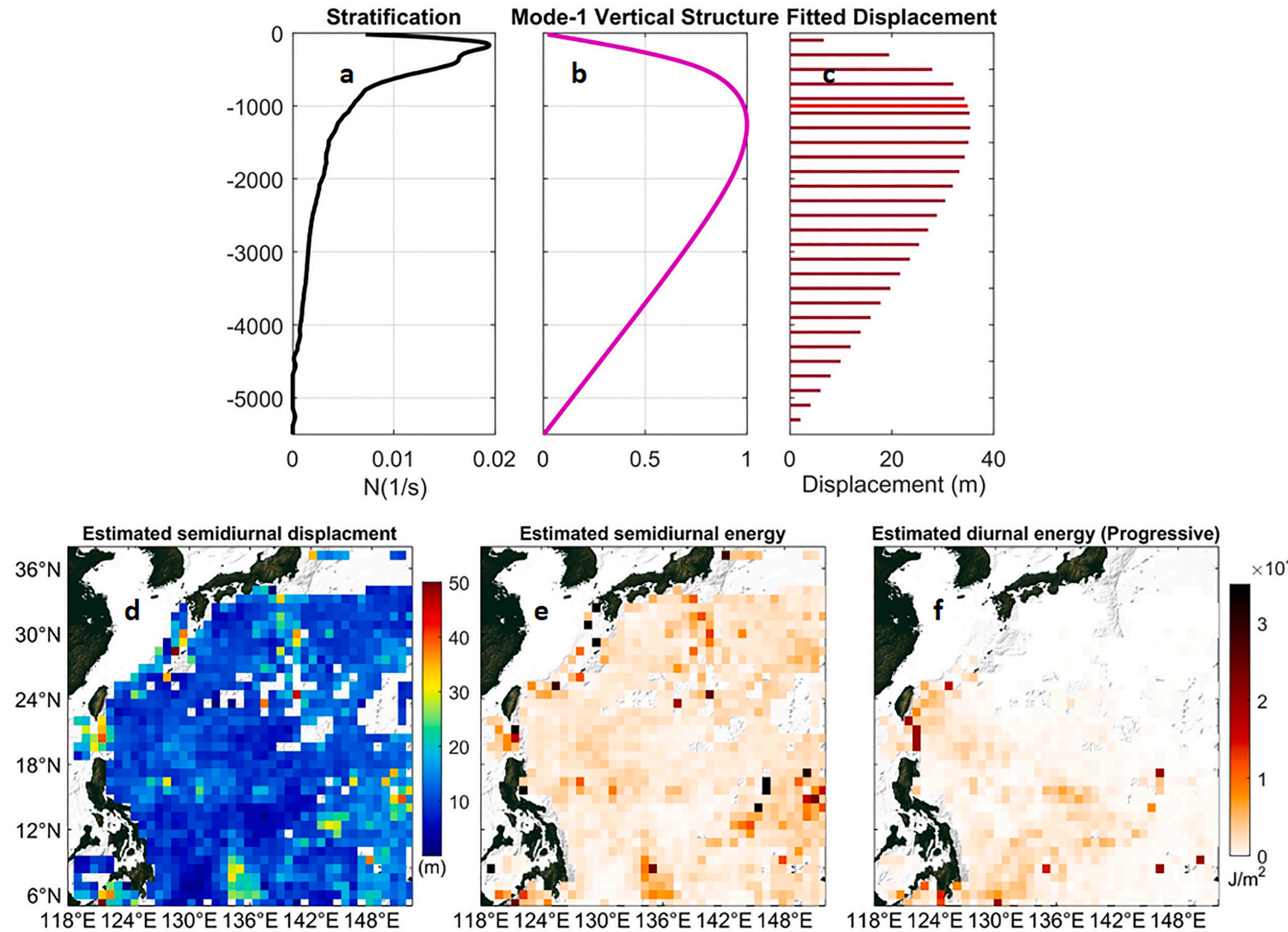

Fig. 10. (a) Time-mean stratification from Argo profiles; (b) Mode-1 internal wave structure; (c) The fitted full-depth displacement, the red line indicates the displacements at the depth of 1000 dbar. (d) The color represents the estimated semidiurnal displacements (unit: dbar); (e) The color represents the estimated semidiurnal energy. (f) As in (e) but for estimated diurnal energy (unit is J/m^2).

The total energy $E = HKE + APE$ for semidiurnal and diurnal internal tide were calculated (Fig. 10e and f). The magnitudes of the semidiurnal internal tide energy at the source regions were $\sim$1–3 $\times$ 10^4 J/m^2, while the energy magnitudes in the deep basin were generally less than 1 $\times$ 10^4 J/m^2. The distribution of semidiurnal energy magnitudes was consistent with that of the displacements, indicating stronger energy near the source regions. The diurnal internal tide energy mainly distributed in the southern part of the study region, with comparable magnitude to that of semidiurnal internal tide near the LS. The energy distribution further indicated the basin-scale redistribution of internal tide energy and the contribution to the remote dissipation.

3.6. Energy decay scale

The energy attenuation rate of internal tides in the open ocean has long been a key question for the development of parameterizations used in climate-scale ocean models (Mackinnon et al., 2017). Here we estimated the energy decay of semidiurnal internal tides in the NW Pacific basin using the calculated energy. First, we determine the longitude-latitude coordinates of the five main generation sources (LS, MY, IZU, MA and PA). Then, for each geographical bin (Fig. 10e), we calculate the distance from this bin to each source and the shortest distance was retained. Then we used a scatter plot and regression to explore relationships between the distances and the semidiurnal internal tidal energy magnitudes.

Note that the assumption here is that the five sources radiate internal tide with comparable magnitude. It would be more accurate if the energy radiating in different directions could be separated to avoid the influence of interference, which has been well applied in altimeter data (Zhao et al., 2016; Alford et al., 2019). In addition, as the semidiurnal beams in NW Pacific mainly radiate in east-west direction and the group velocity $\mathbf{c}_g$ changes only slightly. Considering the relation between

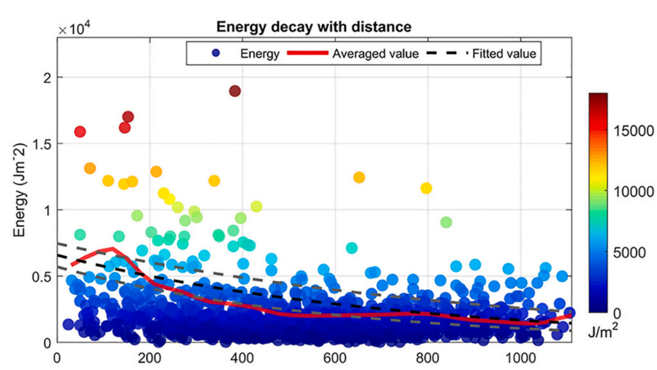

Fig. 11. Scatter plot of the semidiurnal energy with distances (distances away from internal tides sources). The red solid line indicates the averaged energy in bins with distance. The dashed lines indicate the exponential fitted curves. The color denotes the energy magnitude.

energy (E) and energy flux (F): $E = \mathbf{c_g F}$ (Alford and Zhao, 2007; de Lavergne et al., 2019), we estimated the decay of semidiurnal internal tides using the energy.

The semidiurnal internal tidal magnitudes decreased with distance from the generation sites (Fig. 11). In the vicinity of the generation sources, the semidiurnal internal tidal magnitudes reached ~30 kJ/m^2, while in the open ocean, they were much weaker. Using a simple exponential fit to characterize the observed internal tidal energy with distance, the attenuation decreased with increasing distance (black dashed line in Fig. 11). The exponential fit compared well with the averaged values in bins with distance (red solid line in Fig. 11). The e-folding scales of semidiurnal internal tide energy in this region were computed to be ~550–950 km, indicating that the internal tides in the NW Pacific lose 70% of their energy over ~550–950 km. This finding compared favourablly with the altimetric and numerical results of Alford et al. (2019), which suggestted that the e-folding attenuation scale for the southward internal tide beam from Hawaiian Ridge is about 750 km. The decay scale indicated a depth-averaged dissipation rate up to 1.5×10^{-10} W/kg (Alford et al., 2019).

4. Discussion and prospects

One unsatisfying aspect of the calculated displacements was that the insufficient temporal coverage of the data, despite the good spatial coverage. Therefore, we only analyzed the seasonal variation for some selected floats. Moreover, although some floats were equipped with Iridium telecommunication, their drifting cycles at 1000 dbar are only one day or a few days so the diurnal and semidiurnal bands could not be separated.

It can be expected that with an increased number of Iridium Argo floats, the opportunity for a more robust evaluation with better temporal coverage of the basin-scale in-situ observations of internal tides will become feasible in the future. Presently, accurately simulating the internal tidal vertical displacements may be limited by the relatively coarse vertical grid resolution (e.g. at least 50 vertical levels are required to resolve the mode 1 for the z-coordinated models, Stewart et al., 2017) (Carter et al., 2012). This kind of dataset for deep internal tides could also be a good validation for the numerical simulations and for the development of internal tidal models.

By concurrently using both the parking and profiling data of the Iridium-telecommunication Argo floats, direct observation of the deep internal tides on the basin scale becomes more feasible and accurate. This will be an effective and useful supplement to the altimeter satellite data which has been used to reveal the internal tide propagation patterns in recent years (Zhao and Alford, 2009; Zaron, 2019). A recent study also suggested the profiling data could also be used to extract internal wave signals (Hennon et al., 2019). As data accumulate, extraction of both coherent and incoherent internal tidal signals from a longer temporal coverage of the Iridium-telecommunication Argo data will become more feasible.

Most present parameterizations for internal-tide-driven mixing require a key variable which is the local energy available (E_d) for dissipation (St. Laurent et al., 2002; de Lavergne et al., 2019). With the estimated decay scales from the observations, a more accurate E_d can be derived. Combined use of the Iridium-telecommunication Argo observations, altimetry data and numerical models can better characterize the three dimensional internal tide energy fields and contribute to the improvement of ocean models.

5. Summary

We determined the basin-scale pattern and variability of internal tides in the NW Pacific basin using Iridium-communication Argo float data. Strong internal tidal generation sites were identified from the spatial distributions of the vertical displacements at 1000 dbar. Source sites identified included LS, IZU, MA and PA. With some selected floats that remained in a relatively smaller region, the internal tides were found to exhibit seasonal and spring-neap variability.

Furthermore, the Argo float data revealed rich internal tide characteristics. The power spectral shapes displayed different features at different latitudes contributed by different processes. For near source regions, significant energy peaks appeared at semidiurnal and diurnal frequencies. While in the far-field area, the spectra were more consistent with the Garrett-Munk spectrum. We finally gave a preliminary estimation of the e-folding energy attenuation scale as ~550–950 km for the semidiurnal internal tides in the NW Pacific basin, which compared well with previous altimetric results of the southward semidiurnal internal tides from the Hawaiian Ridge (Alford et al., 2019).

The results here give a worthwhile attempt to estimate the attenuation scale for mode-1 internal tidal energy. It should be clear that our estimates have some uncertainties due to some assumptions and data limitations. The far-propagation of internal tides can redistribute the energy available for ocean mixing over a much broader range as revealed by the Argo observations. The results have important implications for improving climatic-scale ocean model parameterizations.

Author contributions

Conceptualization, Y.W. and Z.H.X.; Methodology, Y.W., Z.H.X. and Q.L.; Formal analysis: Y.W.; Writing - Original draft, Y.W.; Writing - Reviewing & Editing, Z.H.X., Q.L., R.R. and B.S.Y.

Declaration of competing interest

The authors declare that they have no known competing financial interests or personal relationships that could have appeared to influence the work reported in this paper.

Data availability

No data was used for the research described in the article.

Acknowledgements

We thank Dr. Jianping Xu and Dr. Genghong Liu for helping accessing the drifting data of the Iridium-telecommunication Argo floats. We thank Dr. Zhongxiang Zhao for the constructive and helpful suggestions. We also thank the International Argo Program and the national programs for conducting the program and making the data available. Funding for this study was provided by the National Natural Science Foundation of China, the Strategic Priority Research Program of Chinese Academy of Sciences, the Scientific and Technological Innovation Project financially supported by Laoshan Laboratory, the National Key Research and Development Program of China (Nos. 92058202, 42006031, XDB42000000, LSKJ202202502, XDA22050202, COMS2020Q07, 2017YFA0604102).

References

Alford, M.H., 2003. Redistribution of energy available for ocean mixing by long-range propagation of internal waves. Nature 423 (6936), 159. https://doi.org/10.1038/nature01628.
Alford, M.H., Zhao, Z., 2007. Global patterns of low-mode internal-wave propagation. Part I: energy and energy flux. J. Phys. Oceanogr. 37 (7), 1829–1848.
Alford, M.H., MacKinnon, J.A., Zhao, Z., Pinkel, R., Klymak, J., Peacock, T., 2007. Internal waves across the pacific. Geophys. Res. Lett. 34 (24).
Alford, M.H., MacKinnon, J.A., Nash, J.D., Simmons, H., Pickering, A., Klymak, J.M., et al., 2011. Energy flux and dissipation in Luzon Strait: two tales of two ridges. J. Phys. Oceanogr. 41 (11), 2211–2222.
Alford, M.H., Peacock, T., MacKinnon, J.A., Nash, J.D., Buijsman, M.C., Centurioni, L.R., et al., 2015. The formation and fate of internal waves in the South China Sea. Nature 521 (7550), 65–69. https://doi.org/10.1038/nature14399.
Alford, M.H., MacKinnon, J.A., Simmons, H.L., Nash, J.D., 2016. Near-inertial internal gravity waves in the ocean. Ann. Rev. Mar. Sci 8, 95–123.

Alford, M.H., Simmons, H.L., Marques, O.B., Girton, J.B., 2019. Internal tide attenuation in the north pacific. Geophys. Res. Lett. 46 (14), 8205–8213. https://doi.org/10.1029/2019GL082648.

Arbic, B.K., Richman, J.G., Shriver, J.F., Timko, P.G., Metzger, E.J., Wallcraft, A.J., 2012. Global modeling of internal tides within an eddying ocean general circulation model. Oceanogr 25 (2), 20–29. https://doi.org/10.5670/oceanog.2012.38.

Bruno, M., Mananes, R., Alonso, J.J., Izquierdo, A., Tejedor, L., Kagan, B.A., 2000. Vertical structure of the semidiurnal tidal currents at Camarinal Sill, the strait of Gibraltar. Oceanol. Acta 23 (1), 15–24.

Buijsman, M.C., Uchiyama, Y., McWilliams, J.C., Hill-Lindsay, C.R., 2012. Modeling semidiurnal internal tide variability in the Southern California Bight. J. Phys. Oceanogr. 42 (1), 62–77. https://doi.org/10.1175/2011JPO4597.1.

Buijsman, M.C., Arbic, B.K., Richman, J.G., Shriver, J.F., Wallcraft, A.J., Zamudio, L., 2017. Semidiurnal internal tide incoherence in the equatorial Pacific. J. Geophys. Res.: Oceans 122 (7), 5286–5305.

Buijsman, M.C., Stephenson, G.R., Ansong, J.K., Arbic, B.K., Green, J.M., Richman, J.G., et al., 2020. On the interplay between horizontal resolution and wave drag and their effect on tidal baroclinic mode waves in realistic global ocean simulations. Ocean Model. 152, 101656.

Cairns, J.L., Williams, G.O., 1976. Internal wave observations from a midwater float, 2. J. Geophys. Res. 81 (12), 1943–1950. https://doi.org/10.1029/JC081i012p01943.

Cao, A., Guo, Z., Lv, X., Song, J., Zhang, J., 2017. Coherent and incoherent features, seasonal behaviors and spatial variations of internal tides in the northern South China Sea. J. Mar. Syst. 172, 75–83.

Carter, G.S., Fringer, O.B., Zaron, E.D., 2012. Regional models of internal tides. Oceanogr 25 (2), 56–65.

Chang, H., Xu, Z., Yin, B., Hou, Y., Liu, Y., Li, D., Liu, A.K., 2019. Generation and propagation of M2 internal tides modulated by the Kuroshio northeast of Taiwan. J. Geophys. Res.: Oceans 124 (4), 2728–2749. https://doi.org/10.1029/2018JC014228.

de Lavergne, C., Falahat, S., Madec, G., Roquet, F., Nycander, J., Vic, C., 2019. Toward global maps of internal tide energy sinks. Ocean Model. 137, 52–75.

Dong, J., Robertson, R., Dong, C., Hartlipp, P.S., Zhou, T., Shao, Z., Chen, J., 2019. Impacts of mesoscale currents on the diurnal critical latitude dependence of internal tides: a numerical experiment based on Barcoo Seamount. J. Geophys. Res.: Oceans 124 (4), 2452–2471.

Duda, T.F., Newhall, A.E., Gawarkiewicz, G., Caruso, M.J., Graber, H.C., Yang, Y.J., Jan, S., 2013. Significant internal waves and internal tides measured northeast of Taiwan. J. Mar. Res. 71 (1–2), 47–81.

Falahat, S., Nycander, J., 2015. On the generation of bottom-trapped internal tides. J. Phys. Oceanogr. 45 (2), 526–545.

Feucher, C., Maze, G., Mercier, H., 2016. Mean structure of the North Atlantic subtropical permanent pycnocline from in situ observations. J. Atmos. Ocean. Technol. 33 (6), 1285–1308.

Fox-Kemper, B., Adcroft, A., Böning, C.W., Chassignet, E.P., Curchitser, E., Danabasoglu, G., Yeager, S.G., 2019. Challenges and prospects in ocean circulation models. Front. Mar. Sci. 6, 65.

Gao, Z., Chen, Z., Huang, X., Xu, Z., Yang, H., Zhao, Z., et al., 2021. Internal wave imprints on temperature fluctuations as revealed by rapid-sampling deep profiling floats. J. Geophys. Res.: Oceans 126, e2021JC017878. https://doi.org/10.1029/2021JC017878.

Garrett, C., Munk, W., 1975. Space-time scales of internal waves: a progress report. J. Geophys. Res. 80 (3), 291–297.

Hennon, T.D., Riser, S.C., Alford, M.H., 2014. Observations of internal gravity waves by Argo floats. J. Phys. Oceanogr. 44 (9), 2370–2386.

Hennon, T.D., Alford, M.H., Zhao, Z., 2019. Global assessment of semidiurnal internal tide aliasing in Argo profiles. J. Phys. Oceanogr. 49 (10), 2523–2533.

Huang, X., Wang, Z., Zhang, Z., Yang, Y., Zhou, C., Yang, Q., Tian, J., 2018. Role of mesoscale eddies in modulating the semidiurnal internal tide: observation results in the northern South China Sea. J. Phys. Oceanogr. 48 (8), 1749–1770.

Jan, S., Chern, C.S., Wang, J., Chao, S.Y., 2007. Generation of diurnal K1 internal tide in the Luzon Strait and its influence on surface tide in the South China Sea. J. Geophys. Res.: Oceans 112 (C6). https://doi.org/10.1029/2006JC004003.

Jan, S., Lien, R.C., Ting, C.H., 2008. Numerical study of baroclinic tides in Luzon Strait. J. Oceanogr. 64 (5), 789–802, 0.1007/s10872-008-0066-5.

Jithin, A.K., Subeesh, M.P., Francis, P.A., Ramakrishna, S.S., 2020. Intensification of tidally generated internal waves in the north-central Bay of Bengal. Sci. Rep. 10 (1), 1–11.

Kelly, S.M., Jones, N.L., Nash, J.D., Waterhouse, A.F., 2013. The geography of semidiurnal mode-1 internal tide energy loss. Geophys. Res. Lett. 40 (17), 4689–4693. https://doi.org/10.1002/grl.50872.

Kerry, C.G., Powell, B.S., Carter, G.S., 2013. Effects of remote generation sites on model estimates of M2 internal tides in the Philippine Sea. J. Phys. Oceanogr. 43 (1), 187–204.

Kerry, C.G., Powell, B.S., Carter, G.S., 2014. The impact of subtidal circulation on internal-tide-induced mixing in the Philippine Sea. J. Phys. Oceanogr. 44 (12), 3209–3224. https://doi.org/10.1175/JPO-D-13-0249.1.

Klymak, J.M., Moum, J.N., 2007. Oceanic isopycnal slope spectra. Part I: internal waves. J. Phys. Oceanogr. 37 (5), 1215–1231.

Klymak, J.M., Alford, M.H., Pinkel, R., Lien, R.C., Yang, Y.J., Tang, T.Y., 2011. The breaking and scattering of the internal tide on a continental slope. J. Phys. Oceanogr. 41 (5), 926–945. https://doi.org/10.1175/2010JPO4500.1.

Lahaye, N., Gula, J., Roullet, G., 2020. Internal tide cycle and topographic scattering over the north mid-atlantic ridge. J. Geophys. Res.: Oceans 125 (12), e2020JC016376.

Legg, S., 2014. Scattering of low-mode internal waves at finite isolated topography. J. Phys. Oceanogr. 44, 359–383.

Li, Z., Storch, J.S.V., Müller, M., 2015. The M2 internal tide simulated by a 1/10° OGCM. J. Phys. Oceanogr. 45 (12), 3119–3135.

Li, Z., von Storch, J.S., Müller, M., 2017. The K1 internal tide simulated by a 1/10° OGCM. Ocean Model. 113, 145–156.

MacKinnon, J.A., Zhao, Z., Whalen, C.B., Waterhouse, A.F., Trossman, D.S., Sun, O.M., Pickering, A., 2017. Climate process team on internal wave–driven ocean mixing. Bull. Am. Meteorol. Soc. 98 (11), 2429–2454. https://doi.org/10.1175/BAMS-D-16-0030.1.

Martini, K.I., Alford, M.H., Nash, J.D., Kunze, E., Merrifield, M.A., 2007. Diagnosing a partly standing internal wave in Mamala Bay. Oahu. Geophys. Res. Lett. 34 (17).

Masunaga, E., Fringer, O.B., Kitade, Y., Yamazaki, H., Gallager, S.M., 2017. Dynamics and energetics of trapped diurnal internal Kelvin waves around a midlatitude island. Journal of Physical Oceanography 47 (10), 2479–2498.

McDougall, T.J., Barker, P.M., 2011. Getting started with TEOS-10 and the Gibbs Seawater (GSW) oceanographic toolbox. SCOR/IAPSO WG 127, 1–28.

Melet, A., Legg, S., Hallberg, R., 2016. Climatic impacts of parameterized local and remote tidal mixing. J. Clim. 29 (10), 3473–3500. https://doi.org/10.1175/JCLI-D-15-0153.1.

Mercier, M.J., Mathur, M., Gostiaux, L., Gerkema, T., Magalhães, J.M., Da Silva, J.C., Dauxois, T., 2012. Soliton generation by internal tidal beams impinging on a pycnocline: laboratory experiments. J. Fluid Mech. 704, 37–60.

Mitchum, G.T., Chiswell, S.M., 2000. Coherence of internal tide modulations along the Hawaiian Ridge. J. Geophys. Res.: Oceans 105 (C12), 28653–28661.

Müller, M., 2013. On the space- and time-dependence of barotropic-to-baroclinic tidal energy conversion. Ocean Model. 72 (Complete), 242–252. https://doi.org/10.1016/j.ocemod.2013.09.007.

Munk, W., Wunsch, C., 1998. Abyssal recipes II: energetics of tidal and wind mixing. Deep-Sea Res. I. 45 (12), 1977–2010.

Musgrave, R.C., MacKinnon, J.A., Pinkel, R., Waterhouse, A.F., Nash, J., Kelly, S.M., 2017. The influence of subinertial internal tides on near-topographic turbulence at the Mendocino Ridge: observations and modeling. J. Phys. Oceanogr. 47 (8), 2139–2154.

Niwa, Y., Hibiya, T., 2001. Numerical study of the spatial distribution of the M2 internal tide in the Pacific Ocean. J. Geophys. Res.: Oceans 106 (C10), 22441–22449.

Niwa, Y., Hibiya, T., 2004. Three-dimensional numerical simulation of M2 internal tides in the East China Sea. J. Geophys. Res.: Oceans 109 (C4). https://doi.org/10.1029/2003JC001923.

Niwa, Y., Hibiya, T., 2011. Estimation of baroclinic tide energy available for deep ocean mixing based on three-dimensional global numerical simulations. J. Oceanogr. 67 (4), 493–502. https://doi.org/10.1007/s10872-011-0052-1.

Oka, A., Niwa, Y., 2013. Pacific deep circulation and ventilation controlled by tidal mixing away from the sea bottom. Nat. Commun. 4 (1), 1–8.

Pickering, A., Alford, M., Nash, J., Rainville, L., Buijsman, M., Ko, D.S., Lim, B., 2015. Structure and variability of internal tides in Luzon Strait. J. Phys. Oceanogr. 45 (6), 1574–1594.

Rainville, L., Pinkel, R., 2006. Propagation of low-mode internal waves through the ocean. J. Phys. Oceanogr. 36 (6), 1220–1236.

Rainville, L., Lee, C.M., Rudnick, D.L., Yang, K.C., 2013. Propagation of internal tides generated near Luzon Strait: observations from autonomous gliders. J. Geophys. Res.: Oceans 118 (9), 4125–4138. https://doi.org/10.1002/jgrc.20293.

Ray, R.D., Cartwright, D.E., 2001. Estimates of internal tide energy fluxes from Topex/Poseidon altimetry: central North Pacific. Geophys. Res. Lett. 28 (7), 1259–1262.

Ray, R.D., Mitchum, G.T., 1996. Surface manifestation of internal tides generated near Hawaii. Geophys. Res. Lett. 23 (16), 2101–2104.

Robertson, R., 2011. Interactions between tides and other frequencies in the Indonesian seas. Ocean Dynam. 61, 69–88. https://doi.org/10.1007/s10236-010-0343-x.

Roemmich, D., Riser, S., Davis, R., Desaubies, Y., 2004. Autonomous profiling floats: workhorse for broad-scale ocean observations. Mar. Technol. Soc. J. 38 (2), 21–29.

Roemmich, D., Alford, M.H., Claustre, H., Johnson, K., King, B., Moum, J., Yasuda, I., 2019. On the future of Argo: a global, full-depth, multi-disciplinary array. Front. Mar. Sci. 6, 439.

Savage, A.C., Arbic, B.K., Richman, J.G., Shriver, J.F., Alford, M.H., Buijsman, M.C., Zamudio, L., 2017. Frequency content of sea surface height variability from internal gravity waves to mesoscale eddies. J. Geophys. Res.: Oceans 122 (3), 2519–2538.

Shanks, A.L., 2021. Observational Evidence and Open Questions on the Role of Internal Tidal Waves on the Concentration and Transport of Floating Plastic Debris. Front. Mar. Sci. 8, 621062.

Sharples, J., Tweddle, J.F., Mattias Green, J.A., Palmer, M.R., Kim, Y.N., Hickman, A.E., Krivtsov, V., 2007. Spring-neap modulation of internal tide mixing and vertical nitrate fluxes at a shelf edge in summer. Limnol. Oceanogr. 52 (5), 1735–1747.

Simmons, H.L., Hallberg, R.W., Arbic, B.K., 2004. Internal wave generation in a global baroclinic tide model. Deep Sea Res. Part II Top. Stud. Oceanogr. 51 (25–26), 3043–3068. https://doi.org/10.1016/j.dsr2.2004.09.015.

Song, P., Chen, X., 2020. Investigation of the internal tides in the Northwest Pacific Ocean considering the background circulation and stratification. J. Phys. Oceanogr. 50 (11), 3165–3188.

Stewart, K.D., Hogg, A.M., Griffies, S.M., Heerdegen, A.P., Ward, M.L., Spence, P., England, M.H., 2017. Vertical resolution of baroclinic modes in global ocean models. Ocean Model. 113, 50–65.

van Haren, H., Duineveld, G., Mienis, F., 2019. Internal wave observations off saba bank. Front. Mar. Sci. 5, 528.

Varlamov, S.M., Guo, X., Miyama, T., Ichikawa, K., Waseda, T., Miyazawa, Y., 2015. M2 baroclinic tide variability modulated by the ocean circulation south of J apan. J. Geophys. Res.: Oceans 120 (5), 3681–3710.

Vic, C., Garabato, A.C.N., Green, J.M., Waterhouse, A.F., Zhao, Z., Melet, A., Stephenson, G.R., 2019. Deep-ocean mixing driven by small-scale internal tides. Nat. Commun. 10 (1), 1–9.

Wang, Y.H., Dai, C.F., Chen, Y.Y., 2007. Physical and ecological processes of internal waves on an isolated reef ecosystem in the South China Sea. Geophys. Res. Lett. 34 (18).

Wang, X., Peng, S., Liu, Z., Huang, R.X., Qian, Y.K., Li, Y., 2016. Tidal mixing in the South China Sea: an estimate based on the internal tide energetics. J. Phys. Oceanogr. 46 (1), 107–124. https://doi.org/10.1175/JPO-D-15-0082.1.

Wang, Y., Xu, Z., Yin, B., Hou, Y., Chang, H., 2018. Long-range radiation and interference pattern of multisource M2 internal tides in the philippine sea. J. Geophys. Res.: Oceans 123 (8), 5091–5112. https://doi.org/10.1029/2018JC013910.

Wang, S., Cao, A., Li, Q., Chen, X., 2021. Reflection of K1 internal tides at the continental slope in the northern South China Sea. J. Geophys. Res.: Oceans 126 (7), e2021JC017260.

Wang, Y., Xu, Z., Hibiya, T., Yin, B., Wang, F., 2021. Radiation path of diurnal internal tides in the northwestern pacific controlled by refraction and interference. J. Geophys. Res.: Oceans 126 (11), e2020JC016972.

Waterhouse, A.F., Mackinnon, J.A., Musgrave, R.C., Kelly, S.M., Pickering, A., Nash, J., 2017. Internal tide convergence and mixing in a submarine canyon. J. Phys. Oceanogr. 47 (2), 303–322.

Whalen, C.B., de Lavergne, C., Garabato, A.C.N., Klymak, J.M., Mackinnon, J.A., Sheen, K.L., 2020. Internal wave-driven mixing: governing processes and consequences for climate. Nat. Rev. Earth Environ. 1 (11), 606–621.

Wilson, C., 2011. Chlorophyll anomalies along the critical latitude at 30 N in the NE Pacific. Geophys. Res. Lett. 38 (15).

Wu, L., Jing, Z., Riser, S., Visbeck, M., 2011. Seasonal and spatial variations of Southern Ocean diapycnal mixing from Argo profiling floats. Nat. Geosci. 4 (6), 363–366.

Xie, X., Shang, X., Chen, G., 2010. Nonlinear interactions among internal tidal waves in the northeastern South China Sea. Chin. J. Oceanol. Limnol. 28 (5), 996–1001.

Xu, Z., Yin, B., Hou, Y., Xu, Y., 2013. Variability of internal tides and near-inertial waves on the continental slope of the northwestern South China Sea. J. Geophys. Res.: Oceans 118 (1), 197–211.

Xu, Z., Yin, B., Hou, Y., Liu, A.K., 2014. Seasonal variability and north–south asymmetry of internal tides in the deep basin west of the Luzon Strait. J. Mar. Syst. 134, 101–112. https://doi.org/10.1016/j.jmarsys.2014.03.002, 10.1016/j.jmarsys.2014.03.002.

Xu, Z., Liu, K., Yin, B., Zhao, Z., Wang, Y., Li, Q., 2016. Long-range propagation and associated variability of internal tides in the South China Sea. J. Geophys. Res.: Oceans 121 (11), 8268–8286. https://doi.org/10.1002/2016JC012105.

Xu, Z., Wang, Y., Liu, Z., McWilliams, J.C., Gan, J., 2021. Insight into the dynamics of the radiating internal tide associated with the kuroshio current. J. Geophys. Res.: Oceans, e2020JC017018.

You, J., Xu, Z., Li, Q., Robertson, R., Zhang, P., Yin, B., 2021. Enhanced internal tidal mixing in the Philippine Sea mesoscale environment. Nonlinear Process Geophys. 28 (2), 271–284.

Yu, X., Ponte, A.L., Elipot, S., Menemenlis, D., Zaron, E.D., Abernathey, R., 2019. Surface kinetic energy distributions in the global oceans from a high-resolution numerical model and surface drifter observations. Geophys. Res. Lett. 46 (16), 9757–9766.

Zaron, E.D., 2019. Baroclinic tidal sea level from exact-repeat mission altimetry. J. Phys. Oceanogr. 49 (1), 193–210. https://doi.org/10.1175/JPO-D-18-0127.1.

Zeng, Z., Brandt, P., Lamb, K.G., Greatbatch, R.J., Dengler, M., Claus, M., Chen, X., 2021. Three-dimensional numerical simulations of internal tides in the Angolan upwelling region. J. Geophys. Res.: Oceans 126 (2), e2020JC016460.

Zhang, P., Xu, Z., Li, Q., You, J., Yin, B., Robertson, R., Zheng, Q., 2022. Numerical simulations of internal solitary wave evolution beneath an ice keel. J. Geophys. Res.: Oceans 127, e2020JC017068.

Zhao, Z., 2014. Internal tide radiation from the Luzon Strait. J. Geophys. Res.: Oceans 119 (8), 5434–5448. https://doi.org/10.1002/2014JC010014.

Zhao, Z., 2018. The global mode-2 M2 internal tide. J. Geophys. Res.: Oceans 123 (11), 7725–7746.

Zhao, Z., 2019. Mapping internal tides from satellite altimetry without blind directions. J. Geophys. Res.: Oceans 124 (12), 8605–8625.

Zhao, Z., Alford, M.H., 2009. New altimetric estimates of mode-1 M2 internal tides in the central North Pacific Ocean. J. Phys. Oceanogr. 39 (7), 1669–1684.

Zhao, Z., D'Asaro, E., 2011. A perfect focus of the internal tide from the Mariana Arc. Geophys. Res. Lett. 38 (14).

Zhao, Z., Alford, M.H., Girton, J.B., Rainville, L., Simmons, H.L., 2016. Global observations of open-ocean mode-1 M2 internal tides. J. Phys. Oceanogr. 46 (6), 1657–1684. https://doi.org/10.1175/JPO-D-15-0105.1.

Zhao, C., Xu, Z., Robertson, R., Li, Q., Wang, Y., Yin, B., 2021. The three dimensional internal tide radiation and dissipation in the Mariana Arc-trench system. J. Geophys. Res.: Oceans 126 (5), e2020JC016502.